High fracture toughness of HfC through nano-scale templating and novel sintering aids

DOI:
10.1111/jace.15956

Document Version
Accepted author manuscript

High Fracture Toughness of HfC Through Nano-scale Templating and Novel Sintering Aids

Wei Hao [a, c], Na Ni [b, c,*], Fangwei Guo [a, c], Fangcheng Cao [a, c], Juan Jiang [a, c], Xiaofeng Zhao [a, c,*], Ping Xiao [a, d]

[a] School of Materials Science and Engineering, Shanghai Jiao Tong University, Shanghai 200240, China

[b] Key Lab of Education Ministry for Power Machinery and Engineering, School of Mechanical Engineering, Shanghai Jiao Tong University, Shanghai 200240, China

[c] Gas Turbine Research Institute, Shanghai Jiao Tong University, Shanghai 200240, China

[d] School of Materials, University of Manchester, MSS Tower, Manchester M13 9PL, UK

[*]Corresponding author: Tel./fax: +86 21 54742561

E-mail address: xiaofengzhao@sjtu.edu.cn (Xiaofeng Zhao) and na.ni@sjtu.edu.cn (Na Ni).

Abstract:

An approach to improve the sintering ability and the fracture toughness of hafnium carbide (HfC) ceramic by designing a unique composite structure is reported. The uniform and ultra-fine HfC nanoparticles (~300 nm) are synthesized at 1450 ºC by vacuum carbonization reaction with the glucose-derived hydrothermal precursor as a carbon source and template. HfC ceramic sintered with a SiCN sintering aid of 15 vol. % possesses a beneficial three-dimensional network microstructure composed of inter-penetrating phases of carbon, SiC and HfC with varied stoichiometry at multi-length scales. The obtained HfC exhibits a higher fracture toughness of 5.5 MPa $m^{1/2}$, which can be attributed to the unique composite structure able to promote stress releases in the crack tip and enhance the resistance to crack propagation.

Keywords: Carbides; Nanoparticles; Spark plasma sintering; Composites; Toughness

1. Introduction

Hafnium carbide (HfC) exhibits high thermodynamic stability with a melting point of ~3900 ºC, high hardness and Young' s modulus, as well as good thermomechanical and thermochemical properties [1-3]. Therefore, it is considered as a promising material for applications of high-temperature electrodes, cutting tools, rocket nozzles, nuclear reactor rods, space/air craft and thermal-field emitters [4-7]. Nevertheless, HfC exhibits a low fracture toughness (1.73-3.40 MPa $m^{1/2}$), which can limit its structural applications in extreme environments [2, 8-9]. An effective way to enhance the fracture toughness of HfC is to incorporate secondary phase materials, such as silicon carbide (SiC) rods, BN, SiC ceramics, refractory metal (Tungsten) to form cermets and other high-temperature carbides, as attempted in some previous studies [10-15]. Cheng et al [8] developed the HfC-SiC/graphite composites, which exhibit a high fracture toughness (9.1 ± 0.5 MPa $m^{1/2}$), however only in the direction perpendicular to their anisotropic lamellar microstructure. HfC-W cermets have a high fracture toughness of 13.7 ± 0.7 MPa $m^{1/2}$, but at a cost of a higher weight and a lower ablation resistance [12, 13]. Carbon nanotubes (CNTs) have also been incorporated into HfC-$MoSi_2$ [16] and SiC-ZrB_2 [30] composites as a toughening phase, respectively. However, CNTs can react with ceramic matrix and form a strong interfacial bonding, which is unfavorable for high toughness. Results from some previous studies also suggest that carbon as a soft phase could be a very effective component to add for improving fracture toughness in ceramics such as SiC [32], ZrB_2-SiC [36] and B_4C [37], but its potential has not been explored in HfC.

Furthermore, a sufficient material density needs to be ensured when improving the fracture toughness of HfC. HfC is difficult to sinter and densify due to the low self-diffusivity and strong covalent bonding of HfC. The fabrication of nanopowders and the addition of sintering aids are common approaches to enhance the sintering ability of ceramics. Nano carbon allotropes, disilicides or other carbides used as sintering aids have been reported for sintering of HfC [14-16, 18]. However, the introduction of these sintering aids have been found to also result in unfavorable microstructure changes, such as abnormal grain growth or formation of different surface defects on HfC grains with fast diffusion and mass transfer rate, which are detrimental to the intrinsic properties of HfC, such as high thermodynamic stability, melting point and good thermomechanical, as well as contribute to the limited fracture toughness of 2.8-4.0 MPa $m^{1/2}$ reported for the sintered material [2, 14]. The polymer-derived silicon carbonitride ceramics (SiCN) are scarcely reported as sintering aids for the synthesis of HfC. SiCN ceramics are composed of amorphous SiCN and amorphous carbon. Amorphous SiCN can decompose into carbon and SiC or Si_3N_4 phase at high temperature [19], which can promote the sintering of the HfC ceramics. In addition, amorphous carbon can promote the densification of HfC by minimizing the oxidation of HfC nanoparticles surface [32].

With the aim of enhancing densification and fracture toughness of HfC simultaneously, we start with a simple method of in-situ vacuum carbonization to synthesize uniform and ultra-fine HfC particles using nano glucose-derived hydrothermal carbon as carbon source as well as a template for HfC formation. The

resulting HfC nano-powders possess preferable nanostructure and stoichiometry, which allows to develop a unique composite microstructure comprising of multiple phases with graded hardness in the dense HfC samples using spark plasma sintering (SPS) with the help of a SiCN sintering aid. The microstructure and mechanical properties of the HfC powders and bulk samples were characterized and the underlying mechanisms for the improved density and fracture toughness are discussed. The approach in this work also shed a light on the design of unique composition and microstructure in UHTC carbides for improved mechanical properties.

2. Experimental Procedure

2.1 Synthesis of the glucose-derived carbon precursor

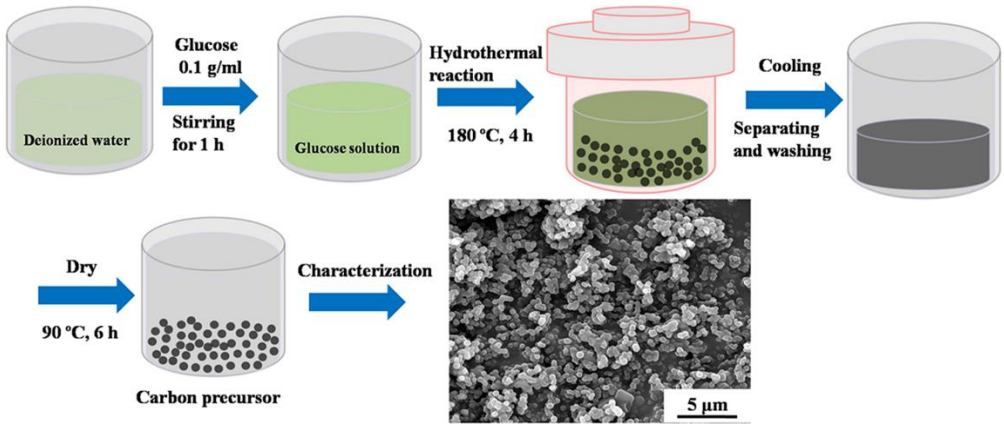

Figure 1 Synthesis process of glucose-derived carbon precursor prepared by hydrothermal pyrolysis.

For the synthesis of HfC nano-powders, glucose-derived carbon precursor with nanometer size and good dispersibility was prepared with glucose using hydrothermal pyrolysis, as schematically shown in Figure 1. Firstly, 5 g anhydrous glucose (purity>99.5%, Sinopharm Chemical Reagent Co., Ltd, China) was dissolved in 50

mL deionized water followed by magnetic stirring for 1 h. Then, the formed precursor solution was transferred into a 50 mL Teflon-lined stainless steel autoclave with the filling capacity of 60 %, which was pre-heated in an oven at 180 ºC. The pyrolysis process of glucose was carried out at 180 ºC for 4 h and the autoclave was cooled down naturally to the room temperature in the open air. Afterwards, the products were filtered and washed with deionized water and dehydrated alcohol for several times, then dried in the drying oven at 60 ºC for 4 h. The final product was the glucose-derived nano-carbon precursor.

2.2 Synthesis of the HfC powders

To synthesize HfC nano-powders, a mixture of the above glucose-derived nano-carbon precursor and hafnium (Hf phase, purity>99 %, mean particle size of 1-2 μm, Shanghai Chao Wei Nano Technology Co. Ltd, China) powders with a mass ratio of $m_{Carbon} : m_{Hf} = 1 : 2$ was loaded into an alumina boat with a cover. The over-stoichiometry of carbon is designed to facilitate the carbonization of Hf and control the particle size and distribution of HfC powders, as will be demonstrated in the results section. This boat was heated in vacuum atmosphere (10^{-4} Pa) at 1300 °C, 1350 °C, 1400 °C, 1450 °C or 1500 °C for 2 h, and then cooled down to the room temperature. The resulting samples are referred from now on as sample #1, #2, #3, #4 and #5, respectively.

2.3 Spark plasma sintering (SPS) of the HfC powders

The HfC powders synthesized at 1450 °C (sample #4) were sintered by a SPS furnace (FTC HP D25, FCT Systeme GmbH, Rauenstein, Germany). Before starting

the experiments, the SPS chamber pressure was kept down to 0 mbar and Argon was introduced to allow pyro-flushing for more stable temperature readings. For the SPS process, the as-prepared HfC powder (4.23 g) was poured into a 16 mm graphite die which was lined with 0.3 mm thick graphite foils to maximize electrical and thermal conduction between the punches and the die. The compacts were heated from room temperature to 1100 °C at a heat rate of 100 °C/min and then heated from 1100 °C to 1850 °C at a heat rate of 50 °C/min. After a dwell time of 15 min at 40 MPa, the furnace was cooled to the room temperature naturally. Furthermore, to investigate the effect of SiCN as a sintering aid in the densification of HfC bulk materials, different HfC ceramic samples were prepared in presence of 0 vol. % and 15 vol. % SiCN, (particle size of 5-8 μm).

2.4 Characterization of the as-synthesized powders and sintered ceramics

The phase compositions of the as-prepared powders and sintered ceramics were characterized by a X-ray diffraction (XRD, Ultima IV, Rigaku) with the Cu Ka radiation (k=0.15406 nm). Raman spectroscopy of the as-prepared samples was performed on the Raman Microprobe (LabRAM HR, Horiba Jobin Yvon, France). A focused laser spot (Nd:YAG, 532 nm) with a diameter of about 3 μm was used. The microstructure and chemical information of the samples were characterized by field emission scanning electron microscopy (FE-SEM, Inspect F50, FEI) and (scanning) transmission electron microscopy ((S)TEM, JEOL JEM 2100F, 200 kV) equipped with a 80 mm silicon drift energy dispersive X-ray spectroscopy (EDX) and a Gatan Tridiem imaging filter for electron energy loss spectroscopy (EELS). The relative

density of the sintered HfC were estimated by the Archimedes method. The total carbon contents within the as-synthesized HfC powders and as-sintered HfC were determined by Element Analyser (G4 ICARUS HF, Bruker AXS, Germany). The determination of the total carbon in the powders is based on the combustion of the sample under flowing dioxygen in an induction furnace at ~3000 °C. The carbon is converted into carbon dioxide which is quantified by an infrared detector. The oxygen content within the as-synthesized HfC powders was analyzed by Element Analyser (ELEMENTRAC ONH-P, Eltra GmbH, Germany).

The HfO_2 content in the as-synthesized HfC powders was calculated with the external standard method from the XRD results, as given in equation (Eq. (1)) [21]:

$$HfO_2\ content\ (wt.\ \%) = \frac{I^S_{(\bar{1}11)}}{I^P_{(\bar{1}11)}} \quad (1)$$

where $I^S_{(\bar{1}11)}$ is the $(\bar{1}11)$-peak intensity of the HfO_2 phase in as-synthesized HfC powder samples; $I^P_{(\bar{1}11)}$ is the $(\bar{1}11)$-peak intensity of the pure HfO_2 reference sample measured under the same conditions. The pure HfO_2 reference sample was prepared with the oxidation of the hafnium powders under 1450 ºC for 2 h in air.

Mechanical properties of the HfC ceramic sample were measured by microindentation tests performed on a microindenter system with a diamond Vickers indenter (Anton Paar, CPX MHT, Austria). The Young's modulus and hardness of the ceramic sample were estimated from the load-displacement curves. A total of 10 indentations with 60 μm interval were made using a load of 1 N with a dwell time of 10 s. For fracture toughness measurements, indentations were performed at a constant

load (10 N) on the well-polished surface of the bulk ceramic samples to induce radial cracking from the corners of the indentation. The lengths of the radial cracks were then measured from the center of indention using SEM. A total of 20 indentations were conducted on each sample. A semi-empirical fracture mechanics analysis of the cracks associated with microindentations yields a measure of toughness, K_{IC}, according to Eq. (2) [10, 36] given as:

$$K_{IC} = \chi(\frac{E}{H})^{1/2} \frac{p}{c^{3/2}} \quad (2)$$

where P is the applied load, N; χ is an empirical constant, H is the hardness, GPa; E is the Young's modulus, GPa and c represents the average crack length determined from the four radial cracks formed from indentations, m.

3. Results and Discussion

3.1 The structure of glucose-derived carbon precursors

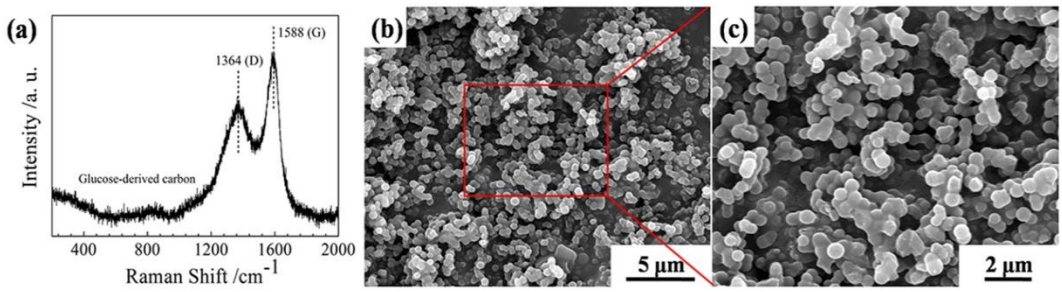

Figure 2 Raman spectrum (a) and SEM images ((b) and (c)) of glucose-derived carbon precursor prepared by hydrothermal method.

The Raman spectrum of the glucose-derived carbon precursor (Figure 2a) displays pyrolysis carbon structure without other impurity peaks. The bands in the position of ~1364 cm^{-1} and ~1588 cm^{-1}, are the D band and G band of the pyrolysis carbon, respectively [22]. The morphology of the glucose-derived carbon precursor exhibits

uniform and small nanoparticles with a size of 200-500 nm (Figure 2b and 2c).

3.2 Phase composition and morphology of as-synthesized HfC powders

Eq. (3-7) describe the chemical reactions expected during the synthesis process.

$$Hf(s) + C(s) \rightarrow HfC(s) \quad (3)$$

$$Hf(s) + O_2(g) \rightarrow HfO_2(s) \quad (4)$$

$$HfO_2(s) + 3C(s) \rightarrow HfC(s) + 2CO(g) \quad (5)$$

$$HfC(s) + O_2(g) \rightarrow HfO_2(s) + C(s) \quad (6)$$

$$2CO(g) + O_2(g) \rightarrow 2CO_2(g) \quad (7)$$

Table 1 The HfO_2 content of as-prepared HfC samples at different carbonization temperatures.

As-prepared powder samples	Carbonization temperatures (°C)	HfO_2 content (wt. %)
1#	1300	21.56 ± 1.34
2#	1350	11.24 ± 0.72
3#	1400	8.46 ± 0.49
4#	1450	4.57 ± 0.23
5#	1500	6.29 ± 0.27

The XRD patterns of the HfC samples (samples #1, #2, #3, #4 and #5) synthesized at different carbonization temperatures (1300-1500 °C) are shown in Figure 3a. Samples #1, #2 and #3 display major cubic HfC (PDF No. 65-8747) structure and a minor monoclinic HfO_2 (PDF No. 65-1142) phase, which indicates that HfC is preferentially formed with respect to HfO_2 according to (Eq. (3) and (4)).

In addition, the peak intensity of the HfC phase increases with the increase of carbonization temperatures until 1450 °C, and that of HfO_2 is highest at 1400 °C. Between 1300 °C and 1400 °C, Hf and HfC can be oxidized to form considerable amount of HfO_2 phase [24]. When carbonization temperature increases to 1450 °C (sample #4), the intensity of HfO_2 peaks are largely reduced and peaks of HfC exhibit the highest intensity, indicating that near pure phase HfC powders are obtained and some of HfO_2 is transformed into HfC and CO (Eq. (5)) at 1450 °C in vacuum [4, 23]. Correspondingly, the HfO_2 content reduces from 8.46 % to 4.57 % at 1450 °C (Table 1). However, when the carbonization temperature is further increased to 1500 °C (Sample #5), the HfC peak intensity of the as-synthesized powders decreases and the HfO_2 content in the sample increases to 6.29 % (Table 1). Additionally, the chemical element analyses show that the as-synthesized HfC powders contain 11.81 wt. % of total C, 2.49 wt. % O and 85.69 wt. % Hf, respectively. The presence of a slight amount of oxygen is attributed to the formation of HfO_2. Due to the presence of residual oxygen, the further oxidation of formed CO is also expected to happen (Eq. (7)).

Raman spectra for the as-synthesized HfC powders with different carbonization temperatures are presented in Figure 3b. Three peaks at 333 cm^{-1}, 578 cm^{-1} and 640 cm^{-1} present in all spectra are assigned to the HfC phase [22]. The peaks at 132 cm^{-1}, 146 cm^{-1}, 240 cm^{-1}, 490 $cm^{-1}$and 795 cm^{-1} are assigned to O-Hf-O bond in HfO_2 [22]. Moreover, the peak intensities for HfC increase while those for O-Hf-O decrease with temperature until 1450 °C. Therefore, the Raman results agree well with the data of

XRD analysis. In addition, Raman spectra indicate the presence of pyrolysis carbon (amorphous carbon) due to the other peaks beyond 1300 cm^{-1} (~1358 cm^{-1} and ~1583 cm^{-1}). This is expected as a result of the reaction of Eq. (6) as well as the residual pyrolysis carbon.

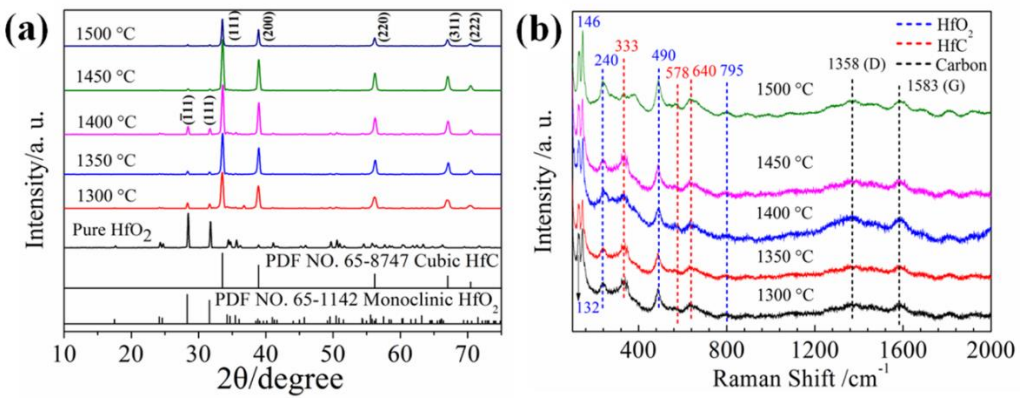

Figure 3 XRD patterns (a) and Raman spectra (b) of HfC powders prepared at different vacuum carbonization temperatures.

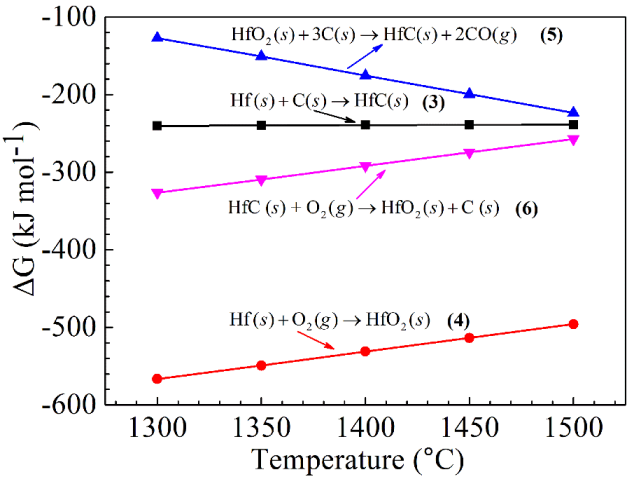

Figure 4 ΔG–T curves for reactions (Eq. (3-6)) on carbonization under vacuum condition (10^{-4} Pa).

The above trend found for the competing formation of HfC and HfO_2 as a function of temperature can be understood by the thermodynamics of carbonization process. The changes in Gibbs-free energy of involved reactions (Eq. (3-6)) at

different carbonization temperatures are calculated according to (Eq. (8-9)) [4]:

$$\Delta G_T^\theta = \sum_i \nu_i \Delta_f G_T^\theta(i) \tag{8}$$

$$\Delta G_T = \Delta G_T^\theta + RT \ln \left[\frac{\prod_f \left(\frac{p_f}{p^\theta} \right)^{\nu_f}}{\prod_r \left(\frac{p_r}{p^\theta} \right)^{\nu_r}} \right] \tag{9}$$

where ΔG_T^θ is the change in Gibbs free energy of the reaction at different temperatures under the standard state, kJ mol^{-1}; ν_i is the coefficient of reactants or products; $\Delta_f G_T^\theta(i)$ is the Gibbs formation free energy for each compound, kJ mol^{-1}. ΔG_T is the change in Gibbs free energy of the reaction at different temperatures under 10^{-4} Pa, kJ mol^{-1}; R is the ideal gas constant, J mol^{-1} K^{-1}; T is temperature, K; p_f is the gas product pressure, Pa; p_r is the gas reactant pressure, Pa; ν_r is the coefficient of reactants; ν_f is the coefficient of products. Δ G–T curves for reactions (Eq. (3-6)) under vacuum condition (10^{-4} Pa) was plotted in Figure 4. As the carbonization temperature increases from 1300 °C to 1500 °C, the Gibbs free energy of the carbothermal reduction reaction (Eq. (5)) decreases rapidly and that of major reaction (Eq. (3)) maintain constant. On the contrary, a fast increase of the Gibbs free energy for the oxidation reactions (Eq. (4) and Eq. (6)) was observed. The calculation indicates the increasing tendency of carbothermal reduction but weakening of HfC oxidation with the increase of temperature. The results are consistent with the XRD and Raman analyses for the decreasing HfO_2 content from 1300 °C to 1450 °C. The enhanced formation of HfO_2 cannot be explained thermodynamically and may be caused by a faster reaction rate of HfC oxidation than that of carbothermal reduction

at higher temperatures.

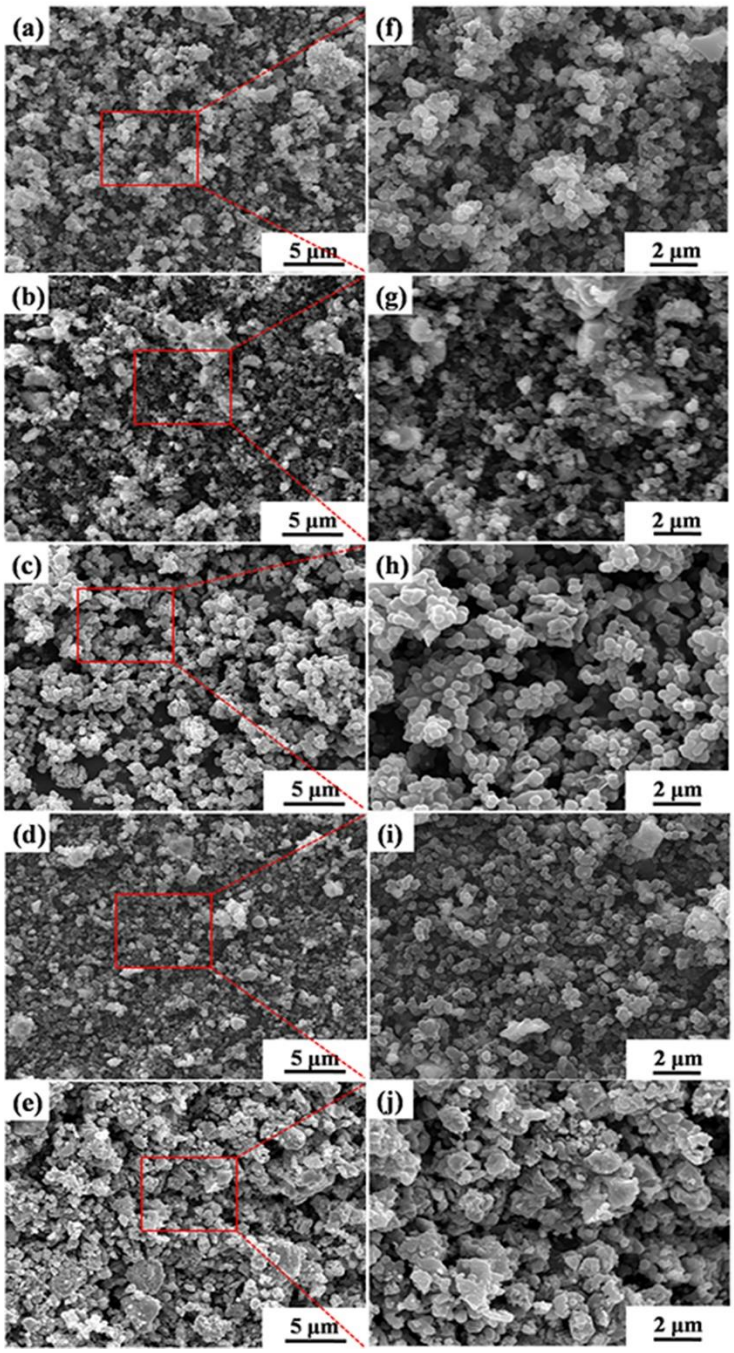

Figure 5 SEM images of as-prepared HfC powders fabricated with different carbonization temperatures. (a, f) 1300 ºC; (b, g) 1350 ºC; (c, h) 1400 ºC; (d, i) 1450 ºC; (e, j) 1500 ºC.

The morphologies of the HfC samples (samples #1, #2, #3, #4 and #5) were

characterized by SEM, as shown in Figure 5. The samples obtained at 1300 ºC and 1350 ºC (sample 1# and 2#) exhibit inhomogeneous particle size and shape with random nanoparticle agglomerations (Figure 5(a, f) and Figure 5(b, g)), indicating an incomplete carbonization reaction during vacuum carbonization process. When carbonization temperature reaches 1400 ºC, more homogeneous and uniform particle size of HfC nanoparticles is synthesized with reduced agglomeration (Figure 5c and Figure 5h). Significantly, most uniform and finest nanoparticles are achieved with a good dispersion at 1450 ºC (Figure 5d and Figure 5i), exhibiting the smallest particle size (~300 nm) among all of the samples. However, when the carbonization temperature increases to 1500 ºC, the as-synthesized HfC sample shows again an inhomogeneous morphology with large bulky particles. The successful preparation of HfC nanoparticles at 1450 ºC and its similar morphology with that of the carbon precursor (Figure 2b and Figure 2c) reveals that small carbon precursor particles not only serve as a carbon source for the carbonization reaction but also act as a template for controlling the particle size and distribution of HfC powders. This mechanism can be attributed to the small carbon precursor particles offering the extended contact area for the reaction with hafnium powders, also limiting growth or agglomeration of the formed HfC particles [4].

The detailed microstructures of the HfC powders synthesized at 1450 ºC were further characterized by TEM. From the low magnification bright field image (Figure 6a), two main contrasts can be observed. The dark phase was identified to be HfC by EDX, high-resolution TEM (HRTEM) and electron diffraction (Figure 6b and Figure

6c). The HfC nanoparticle displays the lattice fringe with a spacing of 0.27 nm corresponding to the (111) plane of cubic HfC phase. The selected area electron diffraction (SAED) pattern from the dark particles (Figure 6c) can be well indexed to the (111), (440), (400) and (200) crystal planes of the cubic HfC phase. This confirms the good crystallinity of the HfC nanocrystals in the HfC powders and is consistent with the XRD analysis. The light contrast regions in Figure 6a are mainly amorphous carbon, however at higher magnifications they were found to contain a high density of Hf enriched HfC particles with a size of only 2-5 nm (Figure 6(e1-e4)). This could result from an evaporation and condensation of Hf during the carbonization process in vacuum. This process may also contribute to the templating effect of the carbon precursor for the ultimate formation of ultra-fine HfC particles.

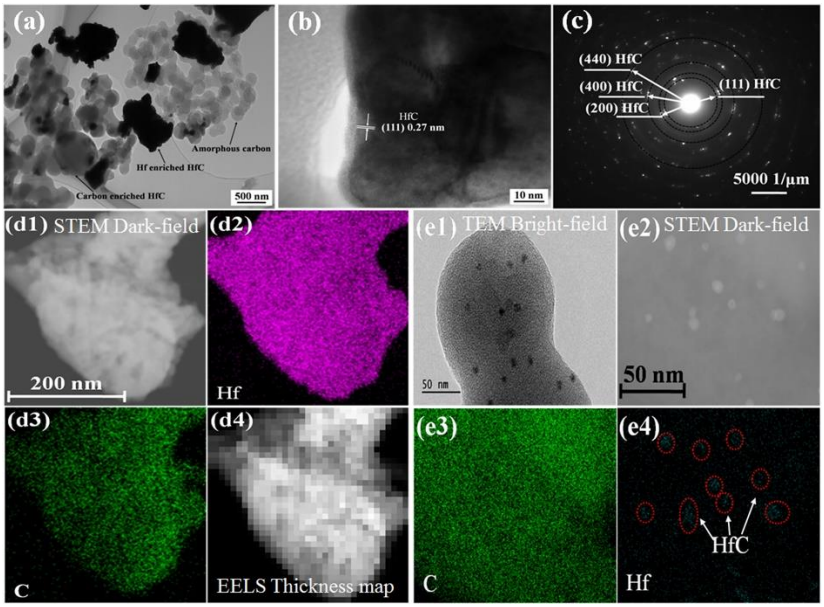

Figure 6 TEM characterization of HfC powders fabricated at 1450 ºC. (a) Low magnification bright field image. (b) HRTEM lattice fringe and (c) SAED of the dark phase shown in (a). (e1) Higher magnification bright field image of the light

amorphous carbon phase shown in (a). (e2-e4) STEM dark field image and EDX element mapping of a similar region showing the amorphous carbon phase contains Hf enriched HfC nanoparticles. (d1-d3) EDX element mapping and EELS relative thickness mapping images of a HfC grain.

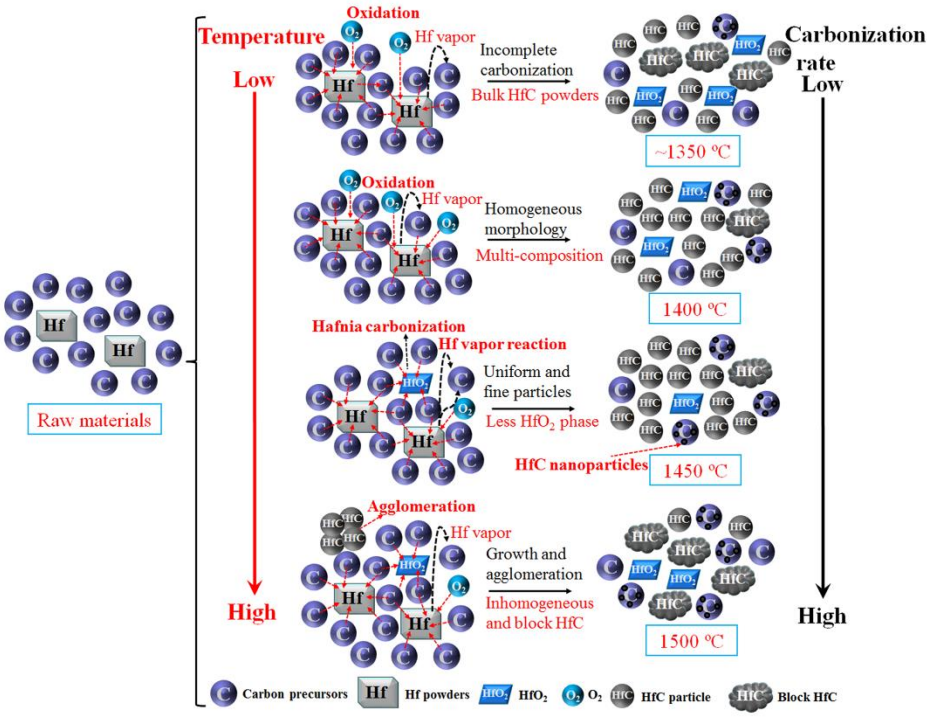

Figure 7 Schematic illustration of the proposed formation mechanisms of HfC crystallines with different carbonization temperatures.

Furthermore, STEM-EDX element mapping ((Figure 6(d1-d4))) revealed that the HfC particles contain carbon rich and deficient regions, indicating a varying stoichiometry of the HfC phase across the sample. The element composition variation in HfC particles was confirmed not to be a result of thickness effect by EELS relative thickness mapping (Figure 6d4), as the compositional variation does not agree with the thickness difference across the region. For simplicity, we will hereafter refer HfC with a relatively higher or lower carbon content as C-enriched or Hf-enriched HfC

respectively, noting that this does not mean over- or sub-stoichiometry of carbon in the phase as no quantification of the exact composition has been made.

Based on the above experimental data, the possible formation mechanisms of HfC at different temperatures are illustrated in Figure 7, where the carbon template-assisted carbonization reaction and the unfavorable oxidation process are both considered. Our results clearly show that carbonization temperature has a significant effect on the resulting morphology of the HfC powders, which should be related to the difference in the rate of HfC nucleation (mostly affected by the thermodynamic barrier of the HfC formation) and diffusion of reactive species. HfC formation through reactions between C and Hf/HfO_2 proceeds mainly via the diffusion of carbon [4, 27]. When the carbonization temperature is below 1400 °C, both the Hf-C for HfC nucleation and the diffusion of carbon precursor are slow. So, the nucleation and growth of HfC happen locally where the contact between Hf and carbon is made, resulting in an incomplete carbonization and inhomogeneous distribution of blocky HfC particles. At ~1400 °C, both the nucleation and growth rates increase, probably to an extent that the two are balanced, leading to a homogeneous distribution of HfC grains with an intermediate size. Moreover, at these low temperatures, Hf oxidation is more thermodynamically favored (Figure 4), resulting in a higher percentage of HfO_2 (Table 1). At 1450 °C, the nucleation and diffusion rates are further increased leading to possibly a faster nucleation than the growth of HfC. HfC crystallites with smaller size and homogeneous distribution can be formed. Additionally, the HfO_2 impurity are carbonized by carbon precursor to form more HfC phase at 1450 °C (Eq. (3-6)) [27].

With the increase of carbonization temperature, Hf evaporation can be enhanced to react with carbon precursors, resulting in the formation of HfC nanoparticles embedded in the carbon precursors. As the carbonization temperature increases to 1500 °C, the highest carbon diffusion rate is expected with an enhanced sintering effect, which leads to overall a slower nucleation than growth of HfC that again causes the coarsening of fine HfC particles.

3.3 Spark plasma sintering of HfC ceramics

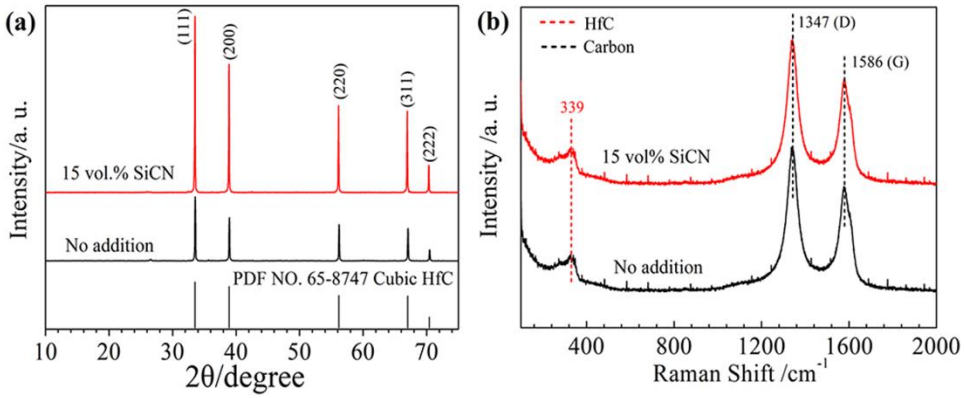

Figure 8 XRD patterns (a) and Raman spectra (b) of as-sintered HfC ceramics prepared with or without sintering aids by SPS.

SPS sintering of the HfC powders was carried out with or without the addition of SiCN. In both cases, XRD analyses (Figure 8a) reveals the presence of cubic HfC (PDF No. 65-8747) structure without HfO_2 or other impurity phases. However, it is clear that the intensities of HfC crystal peaks are higher for the sample sintered with 15 vol. % SiCN than these of HfC ceramics without SiCN, suggesting that the SiCN phase could enhance the crystallization of HfC.

Raman spectra of the sintered HfC ceramics are shown in Figure 8b. The peak at 339 cm^{-1} are assigned to the HfC phase [22, 24], in agreement with the XRD data. In

addition, two peaks at ~1347 cm^{-1} and ~1586 cm^{-1} are assigned to the D band and G band of amorphous carbon [22], suggesting that the amorphous carbon remains after the sintering process. The elemental analysis reveals that the total carbon contents of the sintered HfC-C and HfC-C-15 vol. % SiCN ceramics were 11.45 wt. % and 15.20 wt. %, respectively. The higher total carbon content of HfC-C-15 vol. % SiCN ceramics is mainly due to the introduction of the free carbon in SiCN powders.

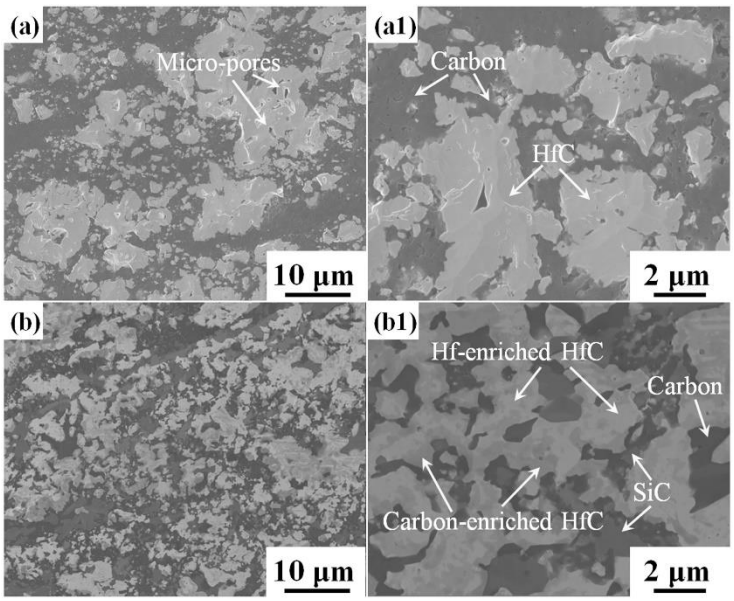

Figure 9 SEM images of as-sintered HfC ceramics prepared with or without sintering aids by SPS. (a, a1) No sintering addition; (b, b1) 15 vol. % SiCN.

Microstructures of the sintered HfC ceramics are compared in Figure 9. The sample sintered without SiCN additions contains more micro-pores and the density was estimated by the Archimedes method to be 7.0 g cm^{-3} with the corresponding relative density of 70.0 % while the one sintered with SiCN additions is denser with a density of 8.76 g cm^{-3} and a relative density of 95.8 %. Bright and dark contrasts were observed in both sintered HfC samples (Figure 9a1 and Figure 9b1), which were

found to be carbon and HfC, respectively. Notably, when the HfC ceramic was sintered with 15 vol. % SiCN, the distribution of the carbon, SiC and HfC phases is much more homogeneous with the size of each phase being ~2 μm (Figure 9b1). Furthermore, it is interesting to note that inside the HfC phase there are again distinctly different contrasts, indicating its varied stoichiometry. This was confirmed by STEM-EDX element mapping and micro-electron diffraction analyses (Figure 10 and Figure S1), which clearly show that Hf/C ratios are different in different HfC grains, forming C-enriched and Hf-enriched HfC phases. This lesds to a homogeneous distribution of different HfC phases at a smaller scale (the size of the HfC phases are down to several hundred nanometers, as evidenced from Figure 9b2 and Figure 10). The TEM analysis also suggests the presence of a very small amount of O in HfC and crystalline SiC (Figure S1). No signal of N could be detected by STEM-EDX within the experimental detection limit in the sintered HfC-SiCN sample and N may have transformed into nitrogen gas and escaped from the sample. So to be more precise, the sintered sample with the SiCN additions contains HfC_xO_y with the HfC crystal structure, crystalline SiC and amorphous carbon.

The above unique microstructure with limited grain growth and inter-penetrating carbon, SiC, C-enriched HfC and Hf-enriched HfC at multi-length scales is considered to result from at least three contributing factors: (1) the presence of C-enriched HfC and Hf-enriched HfC phases in the synthesized HfC nanopowders; (2) the presence of 2-5 nm HfC nanoparticles, which could help to limit the grain growth during the sintering; (3) the introduction of SiCN, which is expected to activate

grain-boundary diffusion and limit grain-boundary migration for the suppression of grain growth [19, 28, 32].

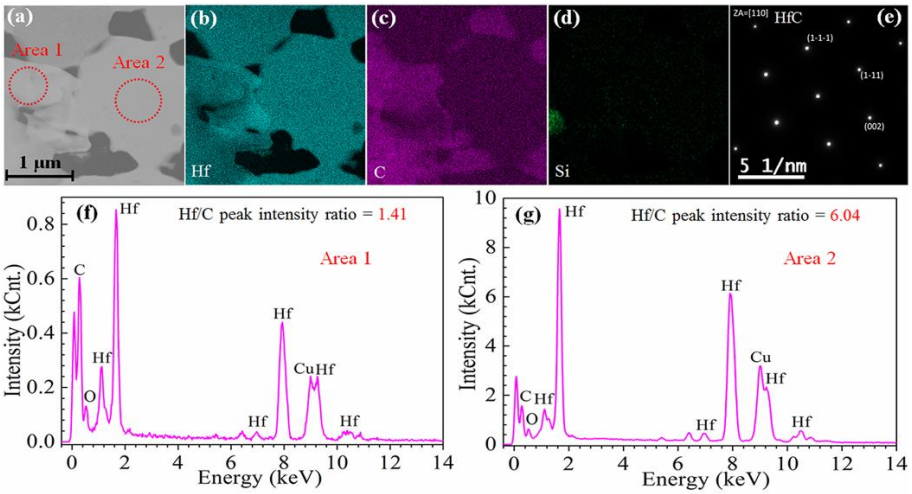

Figure 10 STEM dark field image (a), EDX element mapping (b, c and d), EDX area analyses (f, g) and SAED (e) of as-sintered HfC ceramics with the SiCN 15 vol. % sintering aid by SPS.

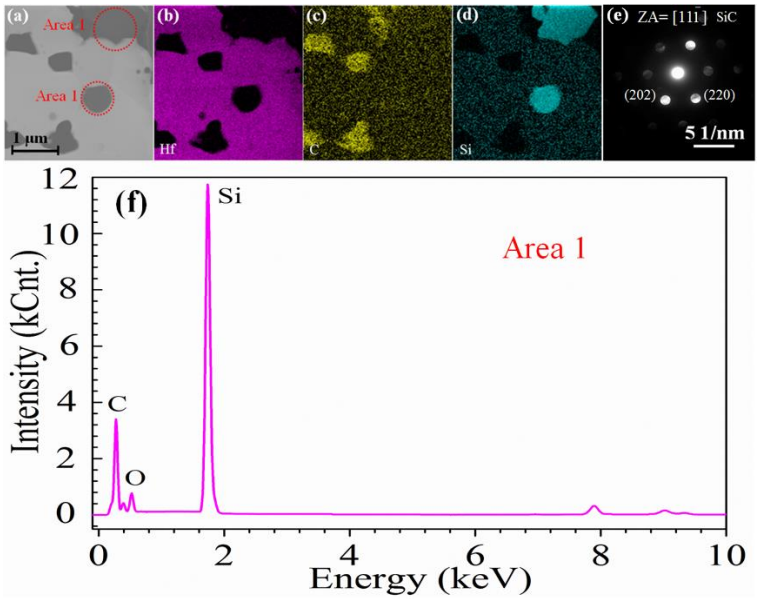

Figure S1 STEM dark field image (a), EDX element mapping (Hf, C and Si) (b-d), SAED (Area 1) (e) and EDX area analyse (Area 1) (f) of the HfC ceramic sintered with 15 vol. % SiCN sintering aid by SPS.

3.4 Young's modulus, hardness and fracture toughness of as-sintered HfC

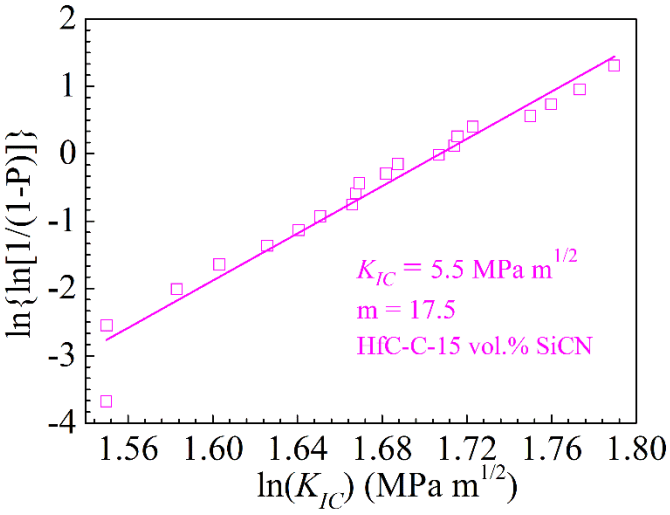

Figure 11 Weibull plots for the measured fracture toughness.

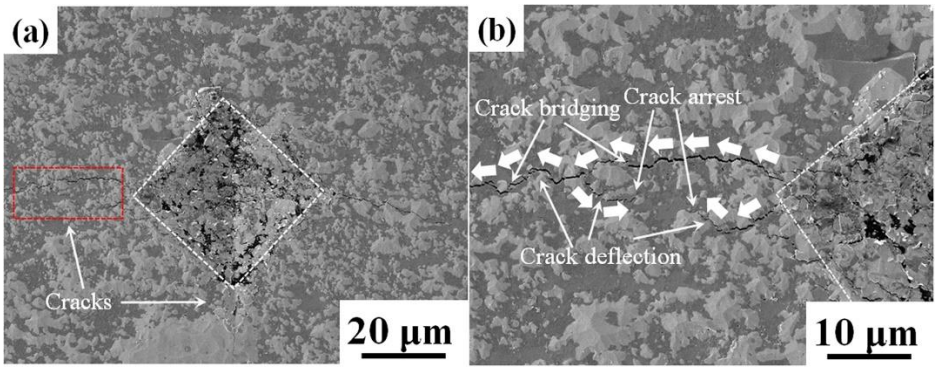

Figure 12 SEM images for indentation cracks on polished surface of HfC ceramic sintered with 15 vol.% SiCN sintering aid by SPS: (a) indentation morphology; (b) the local magnification of (a).

The measured Young's modulus, hardness and fracture toughness of the sintered HfC samples together with some representative literature data are listed in Table 2. In our work, HfC ceramics sintered without the sintering aid possess lower hardness and E than those of other samples in this work and literatures, mainly due to its lower compactness. The mechanical properties of the sintered HfC ceramic are enhanced largely with the addition of 15 vol. % SiCN. The distribution of fracture toughness is

analyzed by the Weibull distribution function. Using Weibull's two-parameter distribution, the cumulative probability of failure (P) is presented as [35]:

$$P = 1 - \exp[-(\frac{K_{IC}}{K_{IC}^*})^m] \quad (9)$$

where K_{IC} is the fracture toughness, MPa $m^{1/2}$; m is the Weibull modulus and K_{IC}^* is the characteristic toughness, MPa $m^{1/2}$. Eq. (9) is usually written in a linear form.

$$\ln\ln(\frac{1}{1-P}) = m\ln(K_{IC}) - m\ln(K_{IC}^*) \quad (10)$$

The failure probability for each tested specimen is usually estimated using:

$$P = \frac{i - 0.5}{N} \quad (11)$$

where N is the number of specimens, the fracture toughness data are organized from weakest to strongest and given a rank i with i=1 being the weakest specimen. Figure 11 shows the measured fracture toughness in the form of Weibull plots. The Weibull modulus is obtained to be 17.5 from the slope. The average value of the fracture toughness is 5.5 MPa $m^{1/2}$. This value is higher than those reported for isotropic HfC or HfC ceramic composites measured by Vickers indentation test [2, 14, 18]. Although some other HfC based composites have been reported to possess a higher fracture toughness, they either had the good property only in a perpendicular direction [8] or used heavy metals as the secondary phase [13], which increases the total weight and degrades the needed high temperature durability of ceramics.

Table 2 The comparison for the hardness, Young's modulus and fracture toughness of as-sintered HfC ceramics from the literature and this work.

Typical ceramic samples	Young's modulus	Hardness	Fracture toughness/K_{IC}	Ref.

	(GPa)	(GPa)	(MPa $m^{1/2}$)	
HfC	360.9±29.5	18.5±0.2	3.4±1.0	[2]
HfC	283±9.6	10.2±0.7	2.9±0.5	[18]
Laminated HfC-SiC/graphite	—	—	9.1±0.5	[8]
SiC rod-reinforced HfC coating	403.7±9.7	21.3±1.0	4.4±0.6	[10]
TaC-30 vol.% HfC -12 vol.% $MoSi_2$	—	15.9±0.6	3.9±0.1	[14]
TaC-30 vol.% HfC -12 vol.% $TaSi_2$	—	17.7±0.4	3.2±0.1	[14]
HfC-W cermets	—	8.8±0.7	13.7±0.7	[13]
HfC-30 vol% SiC	—	20.5±0.2	2.8±0.2	[28]
HfC-C	26.0±2.2	0.9±0.1	—	This work
HfC-C-15 vol.% SiCN	150.6±14.7	5.0±1.1	5.3±0.2	This work

As with most of the ceramics, HfC with relatively higher compactness possess high hardness and Young's modulus, but low fracture toughness. Normal dense HfC is inherently strong but brittle, and often demonstrates extreme sensitivity to flaws [34]. Decreasing the grain size by itself is not as effective in enhancing its fracture toughness as for other ceramic materials, as found for HfC [14], $Ta_{0.8}Hf_{0.2}C$ [15] and TaC-HfC [18]. Consequently, the way to improve the mechanical properties of HfC, especially for its fracture toughness, relies on incorporation of the secondary phases and at the same time the precise control of the microstructure of the sintered materials. In our composite sample, the amorphous carbon with the turbostratic graphite structure (Figure S2) is expected to be the softest [38], and SiC with the bulk hardness

around ~30 GPa is the hardest phase [39]. HfC has the intermediate hardness of ~20 GPa and the varying carbon content is expected to further modify its hardness [40] as what is found for SiC [39]. Therefore, the higher fracture toughness obtained for our samples is believed to be related to the composite structure where multiple phases with different hardness properties form a uniform inter-penetrating 3D network at multi-length scales, a similar approach that many natural biological materials, such as bones, uses to achieve excellent mechanical properties [17]. The observed effect of adding secondary soft phase is also in agreement with previous studies where carbon is used to improve fracture toughness. For example, a SiC-C nanostructure increased the fracture toughness of SiC from 2.4 MPa $m^{1/2}$ to 4.0 MPa $m^{1/2}$ [33]. Additionally, the fracture toughness of ZrB_2-SiC ceramics was improved effectively by incorporating carbon black [37] and the toughness of nanocrystalline boron carbide were improved by introducing soft amorphous carbon at grain boundaries [38].

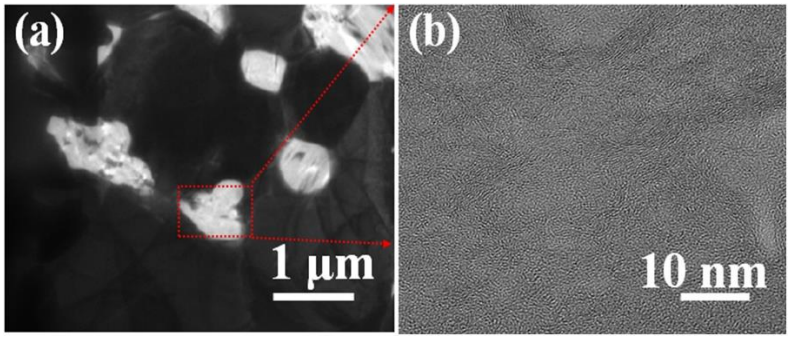

Figure S2 TEM bright field image (a) and HRTEM image for amorphous carbon (b) of the HfC ceramic sintered with 15 vol. % SiCN sintering aid by SPS.

In this work, this approach is optimized to further enhance the fracture toughness by achieving a homogeneous distribution of multiple phases with the graded hardness in a hierarchical structure. As a result, typical crack deflection, bridging and arrest

behavior are observed in our samples for the crack initiated by indentation (Figure 12), which are known to increase the tortuosity of the cracking path and enhance the resistance to crack growth [13, 14], improving the toughness due to the extra energy needed for crack nucleation and propagation.

4. Conclusions

In summary, by effectively combining a facile synthesis of HfC nano-powders and the use of a novel sintering aid in SPS, the sintered HfC ceramics with a unique composite microstructure was successfully fabricated, leading to a greatly enhanced fracture toughness. The following conclusions can be drawn:

(i) The glucose-derived carbon precursor synthesized by hydrothermal method displays pyrolysis carbon structure (amorphous carbon) without other impurity. It exhibits good dispersibility and a fine particle size of 200-500 nm.

(ii) Uniform and fine HfC nanoparticles of ~300 nm were obtained at 1450 ºC by vacuum carbonization of Hf and the carbon precursor nanoparticles. The small carbon precursor not only acts as carbon source but also a template for tailoring the particle size and distribution of HfC powders.

(iii) The as-prepared HfC ceramic sintered with the 15 vol. % SiCN sintering aid possesses a unique composite structure where multiple phases with graded hardness form a uniform inter-penetrating 3D network at multi-length scales. This HfC ceramic sample shows a higher fracture toughness (5.5 MPa $m^{1/2}$) than that of the reported isotropic HfC samples [13, 17]. This preferable microstructure plays a significant role in crack deflection, bridging and arrest, promoting the stress release in the crack tip.

This work suggests that controlling the composition and microstructure to possess graded mechanical properties at different length-scales in UHTCs materials is an effective mechanism and route to improve the mechanical behavior for structural applications.

Acknowledgments

This work has been supported by the National Natural Science Foundation of China (No. 51271120 and 51402058) and the Shanghai Committee of Science and Technology (No. 14ZR1422900 and No. 18PJ1406500).

References

1. Feng L, Lee SH, Wang HL, Lee, HS. Synthesis and densification of nano-crystalline hafnium carbide powder. J Eur Ceram Soc. 2015; 35: 4073–4081.
2. Zhang C, Gupta A, Seal S, Boesl B, Agarwal A. Solid solution synthesis of tantalum carbide-hafnium carbide by spark plasma sintering. J Am Ceram Soc. 2017; 100: 1853–1861.
3. Luo L, Wang YG, Duan LY, Liu LP, Wang GL. Ablation behavior of C/SiC-HfC composites in the plasma wind tunnel. J Eur Ceram Soc. 2016; 36: 3801-3807.
4. Liu JX, Kan YM, Zhang GJ. Synthesis of Ultra-Fine Hafnium Carbide Powder and its Pressureless Sintering. J Am Ceram Soc. 2010; 93: 980–986.
5. Lu DL, Wang WM, Wang H, Zhang JY, Wang YC, Zhang F, et al. Synthesis of ultra-fine hafnium carbide powders combining the methods of liquid precursor conversion and plasma activated sintering. Ceram Int. 2016; 42: 8108–8114.

6. Matović B, Babić B, Bučevac D, Čebela M, Maksimović V, Pantić J, et al. Synthesis and characterization of hafnium carbide fine powders. Ceram Int. 2013; 39: 719–723.

7. Zeng Y, Wang DN, Xiong X, Zhang X, Withers PJ, Sun W, et al. Ablation-resistant carbide $Zr_{0.8}Ti_{0.2}C_{0.74}B_{0.26}$ for oxidizing environments up to 3000 ºC. Nat Commun. 2017; 8: 15826.

8. Xiang LY, Cheng LF, Shi L, Yin XW, Zhang LT. Laminated HfC–SiC ceramics produced by aqueous tape casting and hot pressing. Ceram Int. 2015; 41: 14406–14411.

9. Feng L, Lee SH, Yin J. Low-Temperature Sintering of HfC/SiC Nanocomposites Using $HfSi_2$-C Additives. J Am Ceram Soc. 2016; 99: 2632–2638.

10. Chu YH, Li HJ, Wang YJ, Qi LH, Fu QG. Microstructure and mechanical properties of ultrafine bamboo-shaped SiC rod-reinforced HfC ceramic coating. Surf Coat Technol. 2013; 235: 577–581.

11. Xiang LY, Cheng, LF, Hou Y, Wang FY, Li LJ, Zhang LT. Fabrication and mechanical properties of laminated HfC–SiC/BN ceramics. J Eur Ceram Soc. 2014; 34: 3635–3640.

12. Teague MC, Hilmas GE, Fahrenholtz WG. Reaction Processing of Ultra-High Temperature W/Ta_2C-Based Cermets. J Am Ceram Soc. 2009; 92: 1966–1971.

13. Sun SK, Zhang GJ, Liu JX, Zou J, Ni DW, Cutler R. Reaction Sintering of HfC/W Cermets with High Strength and Toughness. J Am Ceram Soc. 2013; 96: 867–872.

14. Ghaffari SA, Faghihi SMA, Golestani FF, Mandal H. Spark plasma sintering of TaC–HfC UHTC via disilicides sintering aids. J Eur Ceram Soc. 2013; 33: 1479–1484.

15. Ghaffari SA, Faghihi SMA, Golestani FF, Ebrahimi S. Pressureless sintering of $Ta_{0.8}Hf_{0.2}C$ UHTC in the presence of $MoSi_2$. Ceram Int. 2013; 39: 1985–1989.

16. Mukherjeea B, Asiq Rahmana OS, Sribalajia M, Bakshi SR, Keshri AK. Synergistic effect of carbon nanotube as sintering aid and toughening agent in spark plasma sintered molybdenum disilicide-hafnium carbide composite. Mater Sci Eng A. 2016; 678: 299–307.

17. Wegst UG, Bai H, Saiz E, Tomsia AP, Ritchie RO. Bioinspired structural materials. Nat Mater. 2015; 14: 23-36.

18. Cedillos BO, Grasso S, Nasiri NA, Jayaseelan DD, Reece MJ, Lee WE. Sintering behaviour, solid solution formation and characterisation of TaC, HfC and TaC–HfC fabricated by spark plasma sintering. J Eur Ceram Soc. 2016; 36: 1539–1548.

19. Colombo P, Mera G, Riedel R. Polymer-Derived Ceramics: 40 Years of Research and Innovation in Advanced Ceramics. J Am Ceram Soc. 2010; 93: 1805–1837.

20. Klausmann A, Morita KJ, Johanns KE, Fasel C, Durst K, Mera G, et al. Sythesis and high-temperature evolution of polysilylcarbodiimide-derived SiCN ceramic coatings. J Eur Ceram Soc. 2015; 35: 3771-3780.

21. Epp J. X-ray diffraction (XRD) techniques for materials characterization. Mater. Charact. Nondestruct. Eval. (NDE) Meth. 2016: 81-124.

22. Knight DS, White WB. Characterization of diamond films by Raman spectroscopy. J Mater Res. 1989; 4: 385-393.

23. Swift GA, Koc R. Formation studies of TiC from carbon coated TiO_2. J Mater Sci. 1999; 34: 3083-3093.

24. Ramadoss A, Kim SJ. Synthesis and characterization of HfO_2 nanoparticles by sonochemical approach. J Alloy Comp. 2012; 544: 115–119.

25. Shimada S, Yunazar F. Oxidation of Hafnium Carbide and Titanium Carbide Single Crystals with the Formation of Carbon at High Temperatures and Low Oxygen Pressure. J Am Ceram Soc. 2000; 83: 721–728.

26. Shimada S. A thermoanalytical study on the oxidation of ZrC and HfC powders with formation of carbon. Solid State Ion. 2002; 149: 319–326.

27. Yigal DB, Jochen M, David H, Brian A, Michael V. Hafnium Reactivity with Boron and Carbon Sources Under Non-Self-Propagating High-Temperature Synthesis Conditions. J Am Ceram Soc. 2008; 91: 1481–1488.

28. Liu JX, Huang X, Zhang GJ. Pressureless Sintering of Hafnium Carbide–Silicon Carbide Ceramics. J Am Ceram Soc. 2013; 96: 1751–1756.

29. Yadhukulakrishnan GB, Karumuri S, Rahman A, Singh RP, Kalkan AK, Harimkar SP. Spark plasma sintering of graphene reinforced zirconium diboride ultra-high temperature ceramic composites. Ceram Int. 2013; 39: 6637–6646.

30. Scitiw D, Guicciardi S, Nygren M. Densification and Mechanical Behavior of HfC and HfB_2 Fabricated by Spark Plasma Sintering. J Am Ceram Soc. 2008; 91: 1433–1440.

31. Yadhukulakrishnan GB, Rahman A, Karumuri S, Stackpoole MM, Kalkan AK, Singh RP, et al. Spark plasma sintering of silicon carbide and multi-walled carbon nanotube reinforced zirconium diboride ceramic composite. Mater Sci Eng A. 2012; 552: 125–133.

32. Fahrenholtz WG, Wuchina EJ, Lee WE, Zhou YC. Ultra-High Temperature Ceramics: Materials for Extreme Environment Applications, First Edn, New Jersey: The American Ceramic Society. 2014.

33. Lanfant B, Leconte Y, Bonnefont G, Garnier V, Jorand Y, Gallet SL, et al. Effects of carbon and oxygen on the spark plasma sintering additive-free densification and on the mechanical properties of nanostructured SiC ceramics. J Eur Ceram Soc. 2015; 35: 3369–3379.

34. Ritchie RO. The conflicts between strength and toughness. Nat Mater. 2011; 10: 817-822.

35. Satheesh SM, Banerjee A, Bhattacharya E. Determination of polysilicon Weibull parameters from indentation fracture, Thin Solid Films. 2017; 642: 76–81.

36. Quinn GD, Bradt RC. On the Vickers indentation fracture toughness test, J Am Ceram Soc. 2007; 90: 673-680.

37. Zhou SB, Wang Z, Sun X. Microstructure, mechanical properties and thermal shock resistance zirconium diboride containing silicon carbide ceramic toughened by carbon black, Mater Chem Phys. 2010; 122: 470-473.

38. Reddy KM, Guo JJ, shinoda Y, Fujita T, Hirata A, Singh JP, et al. Enhanced mechanical properties of nanocrystalline boron carbide by nanoporosity and

interface phases, Nat Commun. 2012; 3; 1052.

39. Fujiyama H, Nakamura M, Sumomogi T. Mechanical Properties of Silicon Carbide Films Prepared by RF Magnetron Sputtering Using Targets with Different Carbon Contents. American Society for Precision Engineering Proceedings, 2006 Oct 15-20; California, US. 2006.

40. Zeng QF, Peng JH, Oganov AR, Zhu Q, Xie CW, Zhang XD, et al. Prediction of stable hafnium carbides: stoichiometries, mechanical properties, and electronic structure. Phys Rev B. 2013; 88: 214107-(1-6).